A Mass-Conservative Semi-Implicit Semi-Lagrangian Limited-Area Shallow-Water Model on the Sphere

PETER H. LAURITZEN

Department of Geophysics, Niels Bohr Institute for Physics, Astronomy and Geophysics, University of Copenhagen, Copenhagen, Denmark

EIGIL KAAS AND BENNERT MACHENHAUER

Climate Research Division, Danish Meteorological Institute, Copenhagen, Denmark

(Manuscript received 18 February 2005, in final form 27 June 2005)

ABSTRACT

A locally mass conservative shallow-water model using a two-time-level, semi-implicit, semi-Lagrangian integration scheme is presented. The momentum equations are solved with the traditional semi-Lagrangian gridpoint form. The explicit continuity equation is solved using a cell-integrated semi-Lagrangian scheme, and the semi-implicit part is designed such that the resulting elliptic equation is on the same form as for the traditional semi-Lagrangian gridpoint system.

The accuracy of the model is assessed by running standard test cases adapted to a limited-area domain. The accuracy and efficiency of the new model is comparable to traditional semi-Lagrangian methods.

1. Introduction

In atmospheric modeling the accurate and very efficient semi-implicit and semi-Lagrangian (SISL; see appendix A for a complete list of acronyms used in this paper) time-stepping schemes have become popular since their introduction by Robert (1969), Kwizak and Robert (1971), and Robert (1981, 1982), respectively. The popularity is reflected in the large number of meteorological centers that have adopted the SISL schemes for operational models. Until recently a distressing deficiency of semi-Lagrangian models has been their lack of inherent mass conservation, which can result in a significant drift in the global mass field (Moorthi et al. 1995) and most likely can also lead to significant local errors (Machenhauer and Olk 1997). To restore global mass conservation ad hoc a posteriori algorithms may be employed (e.g., Priestley 1993; Gravel and Staniforth 1994; Bermejo and Conde 2002). There is, however, a degree of arbitrariness in the way these "mass fixing" algorithms repeatedly correct the total mass without ensuring the fulfillment of the continuity equation for individual grid cells. In other words, the "mass fixing" algorithms ensure global but not local mass conservation. Recently such local or inherent mass-conserving advection, which also automatically ensures global mass conservation, has been achieved with the development of cell-integrated semi-Lagrangian (CISL) advection scheme (Rančić 1992; Nair and Machenhauer 2002; Nair et al. 2002; Zerroukat et al. 2004b). In these schemes, changes in the total mass of cells moving with the fluid are computed from the continuity equation applied to each cell. CISL schemes are also referred to as finite-volume semi-Lagrangian schemes or semi-Lagrangian remapping schemes (Dukowicz and Baumgardner 2000) in the literature. In addition to being locally mass conservative, accurate, and permitting long time steps, desirable properties such as monotonicity and positive definiteness can easily be enforced when using CISL schemes. To exploit the efficiency of semi-Lagrangian methods in full models it is, however, important to use long time steps, which require a special treatment of the equation terms involved in gravity wave motions, for example, by treating the fast waves semi-implicitly. So far CISL schemes have only been applied to full models using explicit time stepping (e.g., Lin 2004).

Corresponding author address: Peter H. Lauritzen, Climate and Global Dynamics Division, National Center for Atmospheric Research, 1850 Table Mesa Drive, Boulder, CO 80305.
E-mail: pel@ncar.edu

The main novelty of the present study is the coupling of the CISL scheme with a semi-implicit time stepping. A preliminary study was made by Machenhauer and Olk (1997) who derived a one-dimensional SISL shallow-water model based on CISL advection schemes conserving either mass and total energy or mass and angular momentum. The model is yet to be extended to two dimensions and spherical geometry. In one dimension, the derivation of the semi-implicit scheme is rather straightforward but the two-dimensional extension is not obvious. The reason is that the semi-implicit scheme must be consistent with the cell-integrated method, and in two dimensions, this geometric approach leads to a very complicated elliptic system. Instead, we follow a more simple approach suggested by Kaas et al. (2005) for the formulation of a semi-implicit CISL scheme that leads to a simpler elliptic system.

The model presented here is the first step toward a long-term goal: the development of a dynamical core for a global, baroclinic, quasi-hydrostatic, and SISL model that is locally as well as globally mass conserving. In such a model the application of the continuity equation for additional atmospheric constituents on CISL form will automatically guarantee their local mass conservation. Note that if the continuity equation of a dynamical core using a pressure-based vertical coordinate is solved with a numerical method different from a formally mass conservative one used online or offline for tracer transport, the mass of the tracer may not be conserved or the transport may be modeled inaccurately, even if the dynamical core is mass conservative. The problem is caused by the lack of consistency between the mass and wind field, which is explained in detail by Jöckel et al. (2001). A major motivation for the development of a semi-implicit CISL dynamical core is to guarantee consistent online transport of chemical constituents as well as the hydrological variables such as water vapor and cloud water.

In this first step toward the long-term goal, a mass-conserving SISL shallow-water system is set up and tested for a limited area in spherical geometry. The limited-area models (LAMs) cover a rectangular area around the equator of a rotated spherical latitude–longitude grid, which does not include the pole. Hence, the pole problem is not explicitly treated here but possible extensions to a global domain are discussed. The continuity equation is solved using a CISL method on the μ grid, that is, a latitude–longitude grid in which the latitude θ is replaced by $\mu = \sin(\theta)$ (Nair and Machenhauer 2002, hereafter referred to as NM02), whereas the momentum equations are solved using the traditional gridpoint semi-Lagrangian method on a rotated spherical latitude–longitude grid. The semi-implicit continuity equation is formulated such that the resulting elliptic equation is on the same form as for the traditional SISL gridpoint system. The results of test cases with the mass-conservative model are compared to results obtained with a shallow-water version of the traditional nonconserving SISL High Resolution Limited Area Model (HIRLAM) (McDonald and Haugen 1992; McDonald and Haugen 1993).

The mathematical formulation of the traditional semi-Lagrangian method used for the momentum equations and the formulation of the CISL method used for the continuity equation are presented in section 2. The accuracy of the model has been assessed using selected problems from the standard test suite of Williamson et al. (1992, hereafter referred to as W92). The adaptations to a LAM setup and the results from numerical integrations of selected test cases are presented in section 3. Hereafter, possible extensions to a global domain are discussed (section 4) followed by a summary.

2. The model

a. Governing equations

The equations used here are the shallow-water continuity equation

$$\frac{d\Phi}{dt} = -\Phi\nabla\cdot\mathbf{v} \tag{1}$$

and the momentum equations on component form (e.g., McDonald and Bates 1989)

$$\frac{du}{dt} = -\frac{1}{a\cos\theta}\frac{\partial\Phi}{\partial\lambda} + fv, \tag{2}$$

$$\frac{dv}{dt} = -\frac{1}{a}\frac{\partial\Phi}{\partial\theta} - fu, \tag{3}$$

where Φ is the geopotential height, f is the Coriolis parameter, $\mathbf{v}$ is the velocity vector $\mathbf{v} = (u, v)$, d/dt is the horizontal total derivative, ∇ is the horizontal gradient operator, a is the radius of the earth, λ is the longitude, and θ is the latitude. In a semi-Lagrangian model, the trajectory equation

$$\frac{d\mathbf{r}}{dt} = \mathbf{v} \tag{4}$$

is one of the prognostic equations as well. Equations (1)–(4) are the basis for the discretizations in traditional semi-Lagrangian models.

To formulate a CISL continuity equation we integrate (1) over an infinitesimal area δa moving with the

fluid. For consistency the divergence $\nabla \cdot \mathbf{v}$ in (1) must be expressed on the Lagrangian form

$$\mathbb{D} = \frac{1}{\delta a}\frac{d}{dt}(\delta a). \tag{5}$$

Using (5) and integration by parts, (1) becomes the CISL continuity equation

$$\frac{d}{dt}(\Phi \delta a) = 0. \tag{6}$$

The discretizations in the model presented here are based on (2), (3), (4), and (6).

b. Trajectory algorithm

The first step in the semi-Lagrangian algorithm is the computation of the trajectories. The trajectory algorithm used here works directly in (λ, θ) coordinates so $\mathbf{r} = (\lambda, \theta)$. To accommodate the semi-implicit formulation of the continuity equation an iterative departure point algorithm in which the trajectory is split into a part involving only velocities extrapolated to time level $(n + 1)$ and a part involving only velocities at time level (n) is used. This is done by splitting the trajectory into two segments (see Fig. 1):

1) The first contribution is the trajectory from the departure point $\mathbf{r}_*^n$ to the trajectory midpoint $\mathbf{r}_{*/2}^{n+1/2}$. Approximating this half-trajectory with a Taylor series expansion about the departure point, only velocities at time level (n) are used. The Nth-order approximation is given by

$$\mathbf{r}_{*/2}^{n+1/2} = \mathbf{r}_*^n + C_1, \tag{7}$$

where

$$C_1 = \frac{\Delta t}{2}\mathbf{v}_*^n + \sum_{\nu=1}^{N-1}\frac{1}{(\nu+1)!}\left(\frac{\Delta t}{2}\right)^{\nu+1}\left(\frac{d^\nu \mathbf{v}}{dt^\nu}\right)_*^n. \tag{8}$$

The first-guess departure point is the arrival point $\mathbf{r}^{n+1}$. The total derivative is approximated as in McGregor (1993), that is, by discarding the Eulerian velocity change

$$\frac{d\mathbf{v}}{dt} \approx \mathbf{v} \cdot \nabla \mathbf{v}, \tag{9}$$

where the operator ∇ is expressed in spherical coordinates. Higher-order derivatives are defined recursively:

$$\frac{d^\nu \mathbf{v}}{dt^\nu} = \frac{d}{dt}\left(\frac{d^{\nu-1}\mathbf{v}}{dt^{\nu-1}}\right) \quad \nu = 2, 3, \ldots, N-1. \tag{10}$$

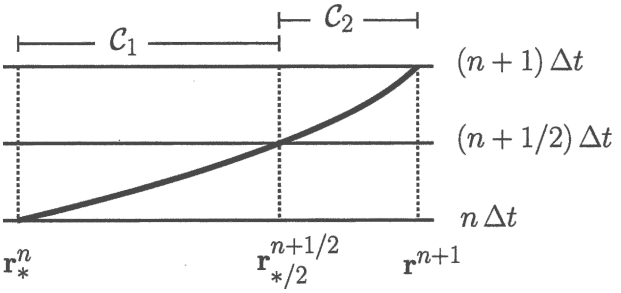

FIG. 1. A space–time diagram (time is plotted on the y axis, and departure point distance is plotted on the x axis) of a trajectory; $\mathbf{r}^{n+1}$ is the arrival point, $\mathbf{r}_*^n$ is the departure point, and $\mathbf{r}_*^{n+1/2}$ denotes the trajectory midpoint. Here C_1 and C_2 are the two contributions to the trajectory. See text for details.

2) The second contribution is the trajectory from the midpoint $\mathbf{r}_{*/2}^{n+1/2}$ to the arrival point $\mathbf{r}^{n+1}$. A Taylor series expansion about the arrival point involves only extrapolated velocities $\tilde{\mathbf{v}}^{n+1}$, where the operator $\widetilde{(\cdot)}^{n+1}$ is defined by

$$\widetilde{(\cdot)}^{n+1} = 2(\cdot)^n - (\cdot)^{n-1}. \tag{11}$$

We have

$$\mathbf{r}_{*/2}^{n+1/2} = \mathbf{r}^{n+1} - C_2, \tag{12}$$

where

$$C_2 = \frac{\Delta t}{2}\tilde{\mathbf{v}}^{n+1} - \sum_{\nu=1}^{N-1}\frac{1}{(\nu+1)!}\left(-\frac{\Delta t}{2}\right)^{\nu+1}\frac{d^\nu}{dt^\nu}(\tilde{\mathbf{v}}^{n+1}). \tag{13}$$

Combining (7) and (12) the departure point is given in terms of the sum of two contributions

$$\mathbf{r}_*^n = \mathbf{r}^{n+1} - (C_1 + C_2). \tag{14}$$

To increase accuracy C_1 is iterated. Note that the second contribution C_2 is based entirely on gridpoint values of the velocity field and is not iterated. We use the first-order $(N = 1)$ approximation to the departure point

$$\mathbf{r}_*^n = \mathbf{r}^{n+1} - \frac{\Delta t}{2}(\mathbf{v}_*^n + \tilde{\mathbf{v}}^{n+1}), \tag{15}$$

for the Lagrangian divergence computations (see below). For all other terms, we include the acceleration $(N = 2)$ for the trajectory computations and use three iterations. For efficiency, bilinear, biquadratic, and bicubic Lagrange interpolation is used for the first, second, and third iteration, respectively. In the present study, we did not investigate if fewer iterations affect the accuracy of the model. This will be the scope of future work.

c. The traditional semi-implicit, semi-Lagrangian discretization

The shallow-water Eqs. (1)–(3) can be written as

$$\frac{d\psi}{dt} = N_\psi + L_\psi; \quad \psi = u, v, \Phi, \tag{16}$$

where L_ψ and N_ψ are the linear and nonlinear parts of the right-hand side of the equation for ψ, respectively. The explicit two-time-level traditional semi-Lagrangian discretization of (16) is given by

$$\psi^{n+1}_{\text{exp}} = \psi^n_* + \Delta t[(L_\psi)^{n+1/2}_{*/2} + (N_\psi)^{n+1/2}_{*/2}], \tag{17}$$

where the known terms have been collected on the right-hand side. Values at time level $(n + \frac{1}{2})$ are obtained by linear extrapolation in time. The classical semi-implicit technique introduced by Robert et al. (1972) treats the nonlinear terms explicitly and the linear part semi-implicitly in terms of a temporal average. The traditional SISL scheme is given by

$$\psi^{n+1} = \psi^n_* + \Delta t(N_\psi)^{n+1/2}_{*/2} + \frac{\Delta t}{2}[(L_\psi)^{n+1} + (L_\psi)^n_*] \tag{18}$$

(e.g., Temperton and Staniforth 1987). It can easily be shown that (18) can be written as

$$\psi^{n+1} = \psi^{n+1}_{\text{exp}} + \frac{\Delta t}{2}\left[(L_\psi)^{n+1} - \widetilde{(L_\psi)^{n+1}}\right], \tag{19}$$

by adding and subtracting $(L_\psi)^{n+1/2}_{*/2}$, using the approximation

$$(L_\psi)^{n+1/2}_{*/2} = \frac{1}{2}\left[(L_\psi)^n_* + \widetilde{(L_\psi)^{n+1}}\right] \tag{20}$$

and (17). Motivated by noise and stability problems, several other ways to evaluate the nonlinear terms have been suggested in the literature. For example, there are the spatially averaged approach where $(N_\psi)^{n+1/2}_{*/2}$ in (18) is replaced by

$$\frac{1}{2}[(N_\psi)^{n+1/2} + (N_\psi)^{n+1/2}_*] \tag{21}$$

(Kaas 1987) and the stable extrapolation two-time-level scheme (SETTLS) used at the European Centre for Medium-Range Weather Forecasts (ECMWF),

$$\frac{1}{2}[2(N_\psi)^n_* - (N_\psi)^{n-1}_* + (N_\psi)^n] \tag{22}$$

(Hortal 2002). The stability of these schemes, and others, is discussed in Durran and Reinecke (2004). Noise problems associated with orographic forcing can also be alleviated by using de-centering (also referred to as uncentering or off-centering in the literature) in which a small off-centering in the time-averaged terms is applied (Rivest et al. 1994).

For the momentum equations, the traditional semi-Lagrangian scheme (19) on an Arakawa C grid (Arakawa and Lamb 1977) with the spatially averaged approximation to the nonlinear terms (21) is used. Treating the continuity equation in the same way, the configuration corresponds to a shallow-water version of the semi-Lagrangian HIRLAM (hereafter referred to as SW-HIRLAM), which will be used for comparison throughout this study. The linear and nonlinear terms are given in appendix B.

d. The discrete CISL continuity equation

The explicit continuity equation is solved in spherical geometry on a μ grid using the discrete form of (6),

$$\overline{\Phi}^{n+1}_{\text{exp}}\Delta A = \overline{\Phi}^n_*\delta A^n, \tag{23}$$

where

$$\overline{\Phi}^n_* = \frac{1}{\delta A^n}\int\int_{\delta A^n}\Phi^n(\lambda, \mu)\, dA \tag{24}$$

is the integral mean value of the geopotential over the irregular departure cell area δA^n, and $\overline{\Phi}^{n+1}_{\text{exp}}$ is the mean value of the geopotential over the regular arrival cell area ΔA. The departure area is defined by tracking backward the trajectories from the corner points of the arrival cell (see, e.g., NM02; Nair et al. 2002). Under the assumption that the time step is chosen such that the trajectories do not cross, the departure cell is "well defined" and the method is guaranteed to be conservative; if cells are not well defined it is detected immediately by the lack of mass conservation. The computation of the integral on the right-hand side of (23) employs two steps. First, the geometry of the departure cell is defined. Second, the remapping is performed, that is, computing the integral over the departure cell using some reconstruction of the subgrid cell distribution at the previous time step. The geometrical definition of the departure cell and the complexity of the subgrid-scale distribution are crucial for the efficiency of the scheme.

In Fig. 2 the departure cells of three different schemes are shown. Rančić (1992) defines the departure cell simply as the quadrilateral resulting from connecting the departure points A, B, C, and D with straight lines (Fig. 2a). For the subgrid-scale distribution, Rančić chose a piecewise biparabolic representation. The scheme, however, was found to be approximately 2.5 times less efficient than the traditional semi-Lagrangian advection scheme. To speed up the

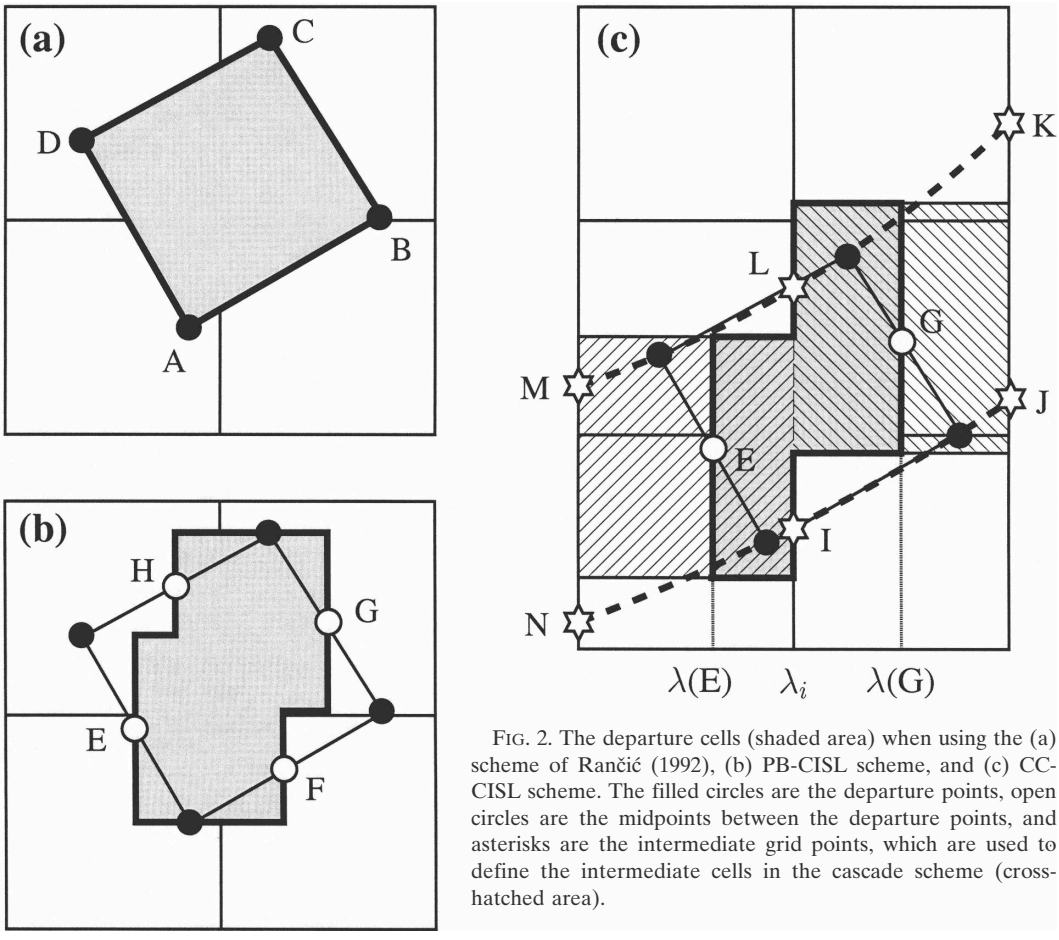

FIG. 2. The departure cells (shaded area) when using the (a) scheme of Rančić (1992), (b) PB-CISL scheme, and (c) CC-CISL scheme. The filled circles are the departure points, open circles are the midpoints between the departure points, and asterisks are the intermediate grid points, which are used to define the intermediate cells in the cascade scheme (cross-hatched area).

remapping process Machenhauer and Olk (1998, 76–85) simplified both the geometry of the departure cell and the subgrid-scale distribution. These simplifications were used in the scheme presented in NM02. The departure cell is defined as a polygon with sides parallel to the coordinate axis (Fig. 2b). The sides parallel to the λ axis are at the μ values of the departure points, and the sides parallel to the μ axis pass through E, F, G, and H, located halfway between the departure points. The biparabolic subgrid-scale representation of Rančić was made pseudo-biparabolic by dropping the "diagonal" terms. Thus, the representation is simply the sum of two one-dimensional parabolic functions, one in each of the two coordinate directions. With this form of departure cell and subgrid-scale distribution the integral over the departure cell can be computed much more efficiently compared to the approach taken by Rančić (1992). For advection in Cartesian geometry, NM02 reported a 10% overhead compared to the traditional semi-Lagrangian scheme. The NM02 scheme is hereafter referred to as the pseudo-biparabolic CISL (PB-CISL) scheme.

The remapping can also be performed by splitting it into two one-dimensional remapping steps using the so-called cascade approach (Purser and Leslie 1991; Rančić 1995; Nair et al. 1999). One such approach is the conservative cascade CISL scheme (CC-CISL) of Nair et al. (2002). In this scheme the departure cells are also defined as polygons with sides parallel to the coordinate axis, and in each one-dimensional cascade step a piecewise parabolic representation is used. Compared to the PB-CISL scheme the departure cell geometry in the CC-CISL scheme is defined somewhat differently (see Fig. 2c). Two of the sides parallel to the μ axis, $\lambda = \lambda(E)$ and $\lambda = \lambda(G)$, are defined as in the PB-CISL scheme and the remaining two sides are at the Eulerian longitude $\lambda = \lambda_i$. The sides parallel to the λ axis are determined from the intermediate Lagrangian grid points I, J, K, L, M, and N defined as $\mu = 1/2\,[\mu(\mathrm{I}) + \mu(\mathrm{J})]$, $\mu = 1/2\,[\mu(\mathrm{K}) + \mu(\mathrm{L})]$, $\mu = 1/2\,[\mu(\mathrm{L}) + \mu(\mathrm{M})]$, and $\mu = 1/2\,[\mu(\mathrm{N}) + \mu(\mathrm{I})]$, respectively. Here the μ values of the intermediate points are determined by a cubic Lagrange interpolation between the μ values of four adjacent departure points along the Lagrangian

latitude (dashed line in Fig. 2c). The upstream integral is computed by a remapping in the north–south direction from the Eulerian cells to the intermediate cells (cross-hatched rectangular regions on Fig. 2c) followed by a remapping along the Lagrangian latitudes from the intermediate cells to the departure cells. Since the two remappings are one-dimensional, the scheme is more than twice as efficient as the PB-CISL scheme (Nair et al. 2002). Another conservative cascade scheme is the one of Zerroukat et al. (2004), which, contrary to the CC-CISL, does not make explicit reference to departure areas during the remapping procedure. Hence, the scheme cannot directly be used in the present model since we make explicit use of areas in the semi-implicit formulation.

Note that all departure areas in Fig. 2 completely cover the entire integration area without overlaps or cracks, and hence the total mass is conserved exactly. The size of the PB-CISL area (Fig. 2c) is equal to that of the Rančić area (Fig. 2b) whereas the CC-CISL area (Fig. 2c) is only approximately so. Therefore, accepting the Rančić definition of the departure area as the most accurate, the PB-CISL area is the most accurate one of the two other schemes. The "jump" in the north and south walls in the CC-CISL scheme is not necessarily midway between the departure points and hence the CC-CISL scheme may conserve mass locally less accurately than the PB-CISL scheme. On the other hand, the CC-CISL scheme may obtain in certain cases a more accurate subgrid-scale representation, namely, when significant variations are along the Lagrangian latitudes and these are sloping toward northeast or southeast. In such situations, the PB-CISL subgrid-scale representation becomes less accurate due to the missing "diagonal" terms. Generally the most accurate subgrid-scale representation of the three schemes is obtained with the full biparabolic representation of Rančić (1992).

As the PB-CISL and CC-CISL scheme use the piecewise parabolic method of Colella and Woodward (1984) for reconstructing the subgrid cell distributions, the monotonic (M), positive-definite (P), and semi-monotonic (SM) constraints as described in Lin and Rood (1996) can optionally be used. In the present model, the PB-CISL and the CC-CISL scheme are used.

To formulate the semi-implicit continuity equation, the Lagrangian divergence (5) is discretized by a centered approximation,

$$\mathbb{D}^{n+1/2} = \frac{1}{\Delta A}\frac{\Delta A - \delta A^n}{\Delta t}. \tag{25}$$

Note that the discretized divergence is determined entirely by the trajectories and the geometrical definition of the departure area. Since the trajectory is split into a part using only extrapolated velocities and velocities at time level (n), the departure area can to first order be split into two parts. The Lagrangian divergence is defined in terms of areas; hence $\mathbb{D}$ can be split into two parts as well:

$$\mathbb{D}^{n+(1/2)} = \frac{1}{2}[\mathbb{D}(\tilde{\mathbf{v}}^{n+1}) + \mathbb{D}(\mathbf{v}^n)]. \tag{26}$$

The first term on the right-hand side of (26) is given by

$$\mathbb{D}(\tilde{\mathbf{v}}^{n+1}) = \frac{1}{\Delta A}\frac{\Delta A - \delta A(\tilde{\mathbf{v}}^{n+1})}{\Delta t}, \tag{27}$$

where the departure area $\delta A(\tilde{\mathbf{v}}^{n+1})$ is computed using only extrapolated winds. As mentioned in section 2b only first-order trajectories (15) are used for the Lagrangian divergence computations, that is, the area is computed using the departure points located at

$$\mathbf{r}^{n+1} - \tilde{\mathbf{v}}^{n+1}\Delta t. \tag{28}$$

For all other terms, the acceleration is included in the trajectory computations.

The ideal semi-implicit continuity equation is derived as in the one-dimensional shallow-water system of Machenhauer and Olk (1997). Isolating δA^n in (25) and thereafter substituting the resulting expression into the explicit continuity Eq. (23), we get

$$\overline{\Phi}^{n+1}_{exp}\Delta A = \overline{\Phi}^{n}_{*}\Delta A - \Delta t\mathbb{D}^{n+1/2}\Phi_{00}\Delta A - \Delta t\mathbb{D}^{n+1/2}\overline{\Phi'}^{n}_{*}\Delta A, \tag{29}$$

where the geopotential $\overline{\Phi}^{n}_{*}$ in the divergence terms has been split into a constant geopotential Φ_{00} and a perturbation $\overline{\Phi'}_{*}$. Treating the linear term semi-implicitly, the ideal semi-implicit continuity equation becomes similar to that of the traditional system:

$$\overline{\Phi}^{n+1} = \overline{\Phi}^{n+1}_{\text{exp}} - \frac{\Delta t}{2}\Phi_{00}[\mathbb{D}^{n+1} - \mathbb{D}(\tilde{\mathbf{v}}^{n+1})]. \tag{30}$$

Since the arrival and departure areas span the entire domain without overlaps or cracks, (30) conserves mass when integrated over the domain when assuming no mass flux through the domain boundaries. Derivation of the full semi-implicit system using (30) and (19) with $\psi = u, v$ requires a formula for the Lagrangian divergence as a function of wind components. This is by no means an impossible task but results in an elliptic equation more complicated than the elliptic equation associated with the traditional system. Rather than pursuing that avenue, we use a predictor-corrector approach that

results in an elliptic equation on the same form as the one associated with the traditional system. Thereby the method is more easily implemented in existing models. The algorithm is an extension to spherical geometry of the algorithm presented in Kaas et al. (2005).

By replacing $\mathbb{D}^{n+1}$ with the discretized Eulerian divergence D^{n+1} in (30), an elliptic equation on the same form as the traditional system results. However, in this context the discretized Eulerian divergence is inconsistent since it corresponds to a discretized Lagrangian divergence with a departure cell area different from that defined for the CISL scheme in question. The "Eulerian" departure cell areas, which correspond to the cell configuration of Laprise and Plante (1995), generally overlap and do not span the entire domain. The inconsistency introduced by using the Eulerian divergence is corrected for in the next time step. The SISL cell-integrated continuity equation becomes

$$\overline{\Phi}^{n+1} = \overline{\Phi}^{n+1}_{\text{exp}} - \frac{\Delta t}{2}\Phi_{00}[D^{n+1} - \mathbb{D}(\tilde{\mathbf{v}}^{n+1})] + \frac{\Delta t}{2}\Phi_{00}\overline{[D^{n} - \mathbb{D}(\mathbf{v}^{n})]}\frac{\delta A^{n}}{\Delta A}. \quad (31)$$

Note that the correction term [last term on the right-hand side of (31)] is integrated over the departure area. The scheme conserves mass both locally and globally. As discussed in connection with the ideal semi-implicit continuity Eq. (30), mass is conserved globally since the Lagrangian divergence terms give no contribution when integrated over the entire domain when assuming no mass flux over the boundaries of the domain. With the same assumption and given that a conservative method is used, the Eulerian divergences D^n and D^{n+1} integrated over the domain both yield zero.

The inconsistent semi-implicit term [second term on the right-hand side of (31)] is corrected for explicitly, which could be a potential source of instability. Numerically we found that by choosing Φ_{00} sufficiently large the scheme is stable for large Courant numbers. A similar condition for stability was derived by Simmons and Temperton (1997) as a result of a stability analysis performed on a two-time-level SISL baroclinic model. They found that the reference surface pressure should be higher than the actual surface pressure in order to have stable integrations. The phase speed of the gravity waves in the model is increased as Φ_{00} is increased, but that is normally of no concern in meteorological applications.

In SW-HIRLAM, as in many atmospheric models, a staggered Arakawa C grid is used. That is, the mass point is situated in the center of a grid cell and the velocity components are situated at the cell sides as indicated on Fig. 3. The principal argument for this choice is that, compared to a nonstaggered A grid with the same resolution, the truncation error of the centered second-order finite-difference approximations for the pressure gradient and the divergence are minimized. To keep our model as close as possible to SW-HIRLAM we also use an Arakawa C grid for the cell-integrated versions. Consequently, the discretization of the momentum equations and the Eulerian divergence used in the correction procedure are as in SW-HIRLAM. In addition, the elliptic equation is on the same form as the one in SW-HIRLAM when a C grid is used.

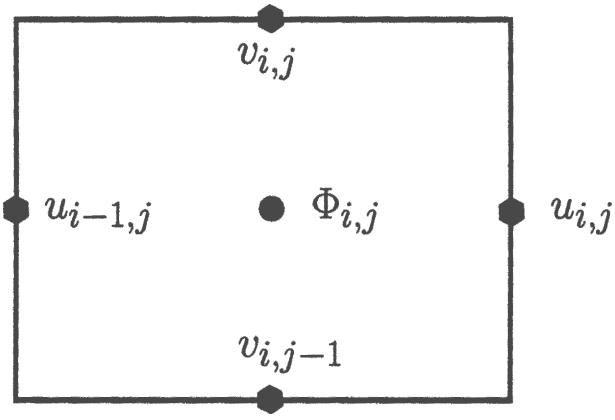

FIG. 3. The placement of the Eulerian cell with respect to the Arakawa C grid.

The algorithm for the cell-integrated models is as follows:

- Interpolate the velocities to cell corner points (using cubic Lagrange interpolation) and compute the trajectories for cell vertices,
- add the correction term

$$\frac{\Delta t}{2}\Phi_{00}[D^{n} - \mathbb{D}(\mathbf{v}^{n})], \quad (32)$$

to $\overline{\Phi}^{n}$ and compute the upstream integral of

$$\overline{\Phi}^{n} + \frac{\Delta t}{2}\Phi_{00}[D^{n} - \mathbb{D}(\mathbf{v}^{n})], \quad \text{and} \quad (33)$$

compute $\mathbb{D}(\tilde{\mathbf{v}}^{n+1})$. Now all known terms on the right-hand side of (31) are computed and the algorithm continues exactly as for the traditional system (e.g., Staniforth and Côté 1991).

Since a "half-implicit Coriolis scheme" is used (see appendix B), the elliptic equation is a Helmholtz equation. It is solved using the solver of HIRLAM, which applies a Fourier transform in the zonal direction

(Källén 1996, p. 2.14). The divergence is assumed zero on the boundaries.

We will refer to the version of the new model as the PB-CISL shallow-water model (PB-CISL-SWM) when using the scheme of NM02 for the continuity equation and the conservative cascade shallow-water model (CC-CISL-SWM) when using the CC-CISL scheme. Note that the Lagrangian divergence is computed according to the departure cell geometry associated with the respective schemes.

3. Results of some tests

The widely accepted test suite proposed by W92 has been used to assess the accuracy of the model. The W92 test cases, however, are formulated for a global domain. Here the tests are run on a limited-area domain, which, of course, requires frequent specification of boundary fields. The analytic solution or a reference solution is used to provide values at the boundaries. But in W92 the reference solutions were only provided daily, which is too infrequent for updating boundary fields in a LAM. Hence, the high-resolution spectral model used in W92 has been rerun to provide boundary data more frequently. A detailed description of the reference solutions and the parameters used for the reference model runs can be found in Jakob et al. (1993).

The LAM uses a rotated spherical latitude–longitude grid. Subsequent reference to the LAM grid refers to the rotated grid and not necessarily to a geographical latitude–longitude grid. The active grid points, that is, grid points at which the solution is computed by the LAM, extend 180° in the longitudinal direction and from 45°S to 45°N on the LAM grid unless stated explicitly otherwise. Around the active domain, there is a halo zone where the reference solution is prescribed. In a 9°-wide zone adjacent to the boundaries of the active domain the solution is relaxed toward the boundary field using a relaxation coefficient, which is decreasing from one to zero over the relaxation zone (Davies 1976). The resolution for the runs is 1.125° unless stated explicitly otherwise. To minimize the errors introduced by the boundary relaxation the boundary fields are updated with the reference solution at every time step. The error measures are computed every hour.

It would be unfair to compare the performance of the LAM to the performance of global models because of the boundary relaxation. Instead a reference shallow-water version of the semi-Lagrangian HIRLAM has been run. SW-HIRLAM uses decentering, filtering of the nonlinear terms in time, and the noise-reducing trajectory scheme of McDonald (1999) (for additional details see section 2c and Undén 2002). For comparison the SW-HIRLAM has been run without decentering as well. The filtering of the nonlinear terms is used in the semi-Lagrangian HIRLAM for stability reasons, but in the tests run here the accuracy was not affected by turning the filter on or off.

For the SW-HIRLAM, we use a constant geopotential Φ_{00} that is equal to the maximum geopotential height of the initial field, $\Phi^0_{\max}$. For the cell-integrated models, we use a constant geopotential that is 10% larger than $\Phi^0_{\max}$ (see discussion in section 2d).

a. Advection experiments (test case 1)

Test case 1 consists of solid-body rotation on the sphere of a cosine bell. For this test case a nonrotated (geographical) grid is used. The wind field is given by

$$u = u_0(\cos\theta\cos\alpha + \cos\lambda\sin\theta\sin\alpha), \tag{34}$$

$$v = -u_0\sin\lambda\sin\alpha, \tag{35}$$

where α is the angle between the axis of solid-body rotation and the polar axis and u_0 is a constant given by

$$u_0 = \frac{2\pi a}{(12\text{ days})}, \tag{36}$$

where $a = 6.37122 \times 10^6$ m is the radius of the earth. W92 proposed advection along the geographical equator ($\alpha = 0.0$) and over the pole ($\alpha = \pi/2$; $\alpha = \pi/2 - 0.05$). These orientations, however, favor the transport scheme since the flow is approximately parallel to the coordinate axis. To complement the results published for the PB-CISL and the CC-CISL schemes, the advection test has been run for $\alpha = 30°$. The flow results in deformed departure cells, which make the problem more challenging than if the departure cells would be rectangles as is the case for $\alpha = 0.0$. The cell deformations affect the upstream integral and divergence computations. For this experiment a global domain in the east–west direction and a resolution of 2.8125° × 2.8125° are used.

Standard nondimensional error measures (see, e.g., W92) for the advection test for different schemes are listed in Table 1. As expected the errors have increased compared to advection for $\alpha = 0.0$ (cf. to Table 1 in Nair et al. 2002). In general the CC-CISL outperforms the PB-CISL scheme. This is because the subgrid-scale representation in the PB-CISL scheme eliminates the cross terms and therefore only includes variation along Eulerian latitudes and longitudes. The CC-CISL scheme may in certain cases include some of the diagonal variation since the second remapping is along the Lagrangian latitudes. In the present case the northern part of the cosine bell is compressed in the (λ, μ) coordinate system as it approaches the most northern po-

TABLE 1. Standard nondimensional error measures for solid-body rotation of a cosine bell for the PB-CISL scheme, the CC-CISL, and the traditional semi-Lagrangian (TRAD) scheme using bicubic Lagrange interpolation, respectively. The angle between the axis of solid-body rotation and the polar axis is 30°, the resolution is 2.8125°, and one revolution is completed in 256 time steps. The letters P, M, and SM denote positive-definite, monotonic, and semimonotonic options, respectively (Lin and Rood 1996). The monotonic filter for TRAD is described in Bermejo and Staniforth (1992). Exact trajectories were used.

Scheme	l_1	l_2	l_∞	Min	Max
PB-CISL	0.075	0.051	0.083	−0.0088	−0.083
CC-CISL	0.051	0.039	0.076	−0.0070	−0.076
PB-CISL-P	0.043	0.040	0.082	−0.00079	−0.082
CC-CISL-P	0.033	0.034	0.077	0.0	−0.077
PB-CISL-M	0.077	0.089	0.18	−0.0038	−0.18
CC-CISL-M	0.070	0.086	0.186	0.0	−0.186
PB-CISL-SM	0.047	0.041	0.082	−0.0032	−0.082
CC-CISL-SM	0.035	0.034	0.076	0.0	−0.076
TRAD	0.25	0.15	0.15	−0.017	−0.151
TRAD-M	0.25	0.19	0.22	0.0	−0.217

sition and vice versa for the most southern position. Obviously, this asymmetry is better resolved along sloping Lagrangian latitudes than along the Eulerian latitudes. When enforcing the P and SM filters, the accuracy is improved. On the other hand, the M filter severely damps and decreases the accuracy. It may be possible to improve the monotonicity filter by adapting the filter of Zerroukat et al. (2005) to the piecewise parabolic method. Note also that 1D filters that prevent under- and overshoots in one dimension do not necessarily guarantee these properties when applied in each coordinate direction to the pseudo-biparabolic subgrid cell representation of the PB-CISL scheme. In the case of negative values at the boundaries of both unfiltered 1D parabolic representations of a cell an even larger negative value may be present in one or more of the cell corners when the 1D representations are added. The 1D M, P, and SM filters eliminate only the negative values at the boundaries and not the larger negative corner values. The same has been observed with the scheme of Lin and Rood (1996) and by NM02. The cascade scheme does not produce negative values after the application of the M, P, or SM filter since the two 1D parabolic representations are applied successively and are never added. Using either the PB-CISL or CC-CISL scheme the accuracy is greatly improved compared to the traditional semi-Lagrangian scheme.

For a nondivergent flow the advection of a constant, for example, Φ_{00}, should ideally yield Φ_{00} at all times. It is well known that CISL schemes do not have this property due to the approximation of the departure cell,

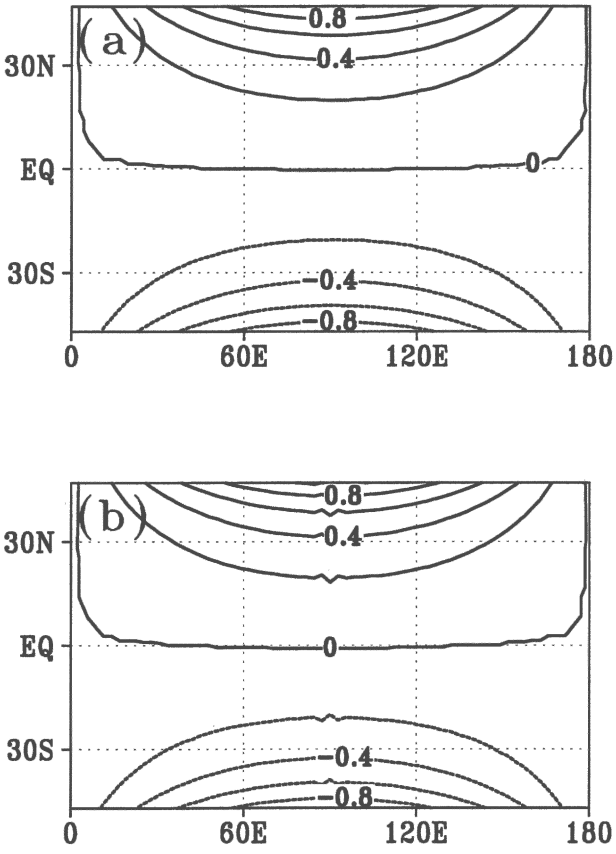

FIG. 4. The constant geopotential $\Phi_{00} = 50\,000\ \mathrm{m^2\,s^{-2}}$ has been advected one time step ($\Delta t = 4050$ s) using the solid-body rotation flow of test case 1. The figure shows the deviation from Φ_{00} when using the (a) PB-CISL and (b) CC-CISL scheme, respectively. The contour interval is $0.2\ \mathrm{m^2\,s^{-2}}$.

which fails to preserve the area exactly (e.g., Laprise and Plante 1995). Consequently, the Lagrangian divergence computations are not strictly correct whereas the Eulerian formula for divergence yields zero at the machine precision. To investigate the severity of the problem the constant field $\Phi_{00} = 50\,000\ \mathrm{m^2\,s^{-2}}$ has been advected one time step in the solid-body rotation flow of test case 1. The results for $\Delta t = 4050$ s are shown in Fig. 4. The errors introduced by the inaccuracies in the departure cell approximations are of the order of 1 $\mathrm{m^2\,s^{-2}}$ for both CISL schemes. Compared to Φ_{00} these errors are considered small.

b. Nonlinear geostrophic flow (test case 2)

The flow field is a geostrophically balanced flow given by (34), (35), and

$$\Phi = gh_0 - \left(a\Omega u_0 + \frac{u_0^2}{2}\right) \times (-\cos\lambda\cos\theta\sin\alpha + \sin\theta\cos\alpha)^2, \qquad (37)$$

TABLE 2. Standard nondimensional error measures for the geopotential height field after 10 days of simulation for test case 2. See text or appendix A for definition of the acronyms. The maximum Courant number is approximately 3.5 for all resolutions, which corresponds to a time step of 900, 1800, and 3600 s for the high-, medium-, and low-resolution runs, respectively.

Model	Resolution (°)	$l_1(h)$	$l_2(h)$	$l_\infty(h)$
SW-HIRLAM	0.5625	3.973E-6	5.931E-6	1.753E-5
SW-HIRLAM no decentering	0.5625	2.126E-6	2.645E-6	6.640E-6
PB-CISL-SWM	0.5625	1.872E-6	2.242E-6	3.701E-6
CC-CISL-SWM	0.5625	2.044E-6	2.453E-6	4.372E-6
SW-HIRLAM	1.125	1.231E-5	1.768E-5	5.077E-5
SW-HIRLAM no decentering	1.125	6.880E-6	1.036E-5	3.863E-5
PB-CISL-SWM	1.125	5.298E-6	6.871E-6	1.766E-5
CC-CISL-SWM	1.125	5.960E-6	7.613E-6	1.868E-5
SW-HIRLAM	2.25	4.829E-5	7.243E-5	2.195E-4
SW-HIRLAM no decentering	2.25	5.607E-5	5.607E-5	2.099E-4
PB-CISL-SWM	2.25	2.635E-5	3.703E-5	9.719E-5
CC-CISL-SWM	2.25	2.844E-5	3.944E-5	9.820E-5

where g is the acceleration due to gravity, $g\,h_0$ is a constant set to 29 400 $m^2\,s^{-2}$, and Ω is the rotation rate of the earth. Ideally, the numerical solution should not change in time. Again a geographical grid is used and $\alpha = 30°$. Since an analytic solution exists the problem is well suited for verifying the convergence of the numerical algorithm. In the context of the PB-CISL scheme the test case is quite useful. As discussed the PB-CISL algorithm favors flow, which is either along longitudes or latitudes, which is not the case in this experiment, and second it serves to investigate if the errors in the Lagrangian divergence computations cause problems for the semi-implicit scheme.

Standard nondimensional error measures for test case 2 are listed in Table 2 for different model configurations and resolutions. As expected, all models converge. The accuracy of the mass-conservative models is significantly better than the accuracy of the SW–HIRLAM. The difference between the error measures of the CISL models is small and probably insignificant given that only a limited area is considered.

c. *Flow over an isolated mountain (test case 5)*

Test case 5 consists of the fields of test case 2 with $u_0 = 20\ m\,s^{-1}$ and $h_0 = 5960$ m and a surface orography given by

$$h_s = h_{s0}\left(1 - \frac{r}{R}\right), \tag{38}$$

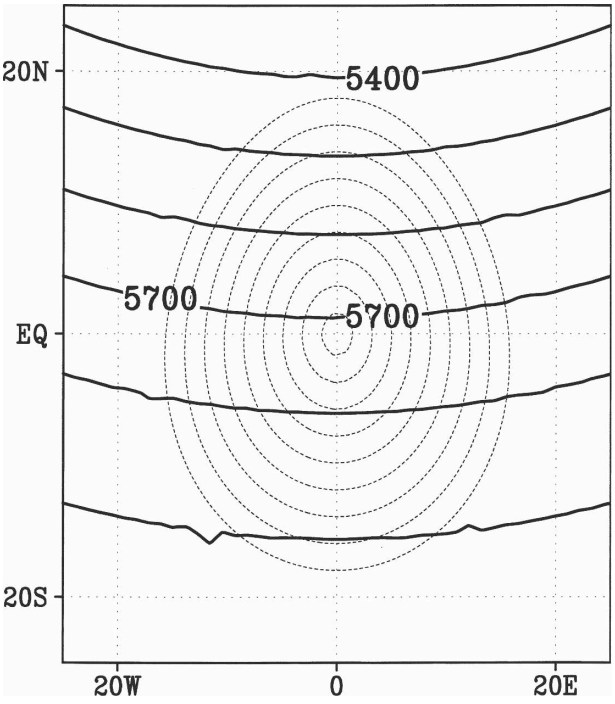

FIG. 5. (solid contours) The initial height field constructed on the LAM grid using the spectral coefficients of the T213 reference solution for test case 5. The LAM grid is a rotated grid and the axis labels denote location on the LAM grid. Only part of the integration domain is shown. The solid-line contour interval is 100 m. (dashed contours) The geopotential height of the orography, Φ_s. The dashed-line contours start at 2000 $m^2\,s^{-2}$ and increase monotonically to 20 000 $m^2\,s^{-2}$ with an increment of 2000 $m^2\,s^{-2}$. Note the noise in the height field near the rim of the mountain. The maximal deviation from the analytical initial condition is approximately 100 $m^2\,s^{-2}$.

where

$$h_{s0} = 2000\ \text{m}, R = \pi/9, \quad \text{and}$$
$$r^2 = \min[R^2, (\lambda - \lambda_c)^2 + (\theta - \theta_c)^2], \tag{39}$$

where $(\lambda_c, \theta_c) = (3\pi/2, \pi/6)$. The rotated south pole is located at 60°S, 270°W so that the peak of the mountain is at the origin of the LAM grid. The initial condition on the LAM grid is shown in Fig. 5. There is no analytic solution to this problem so the high-resolution spectral model is used to produce a reference solution. The representation of the mountain, however, is a challenge for the spectral scheme due to Gibbs's phenomena. As shown in Fig. 5 small-scale noise is present near the rim of the mountain already in the initial state. The maximum difference in the geopotential height field between the analytic initial condition and the initial condition constructed using spectral coefficients is approximately 100 $m^2\,s^{-2}$. In addition to the inaccuracies introduced by Gibbs's phenomena, the flow will initially experience an abrupt change due to the presence

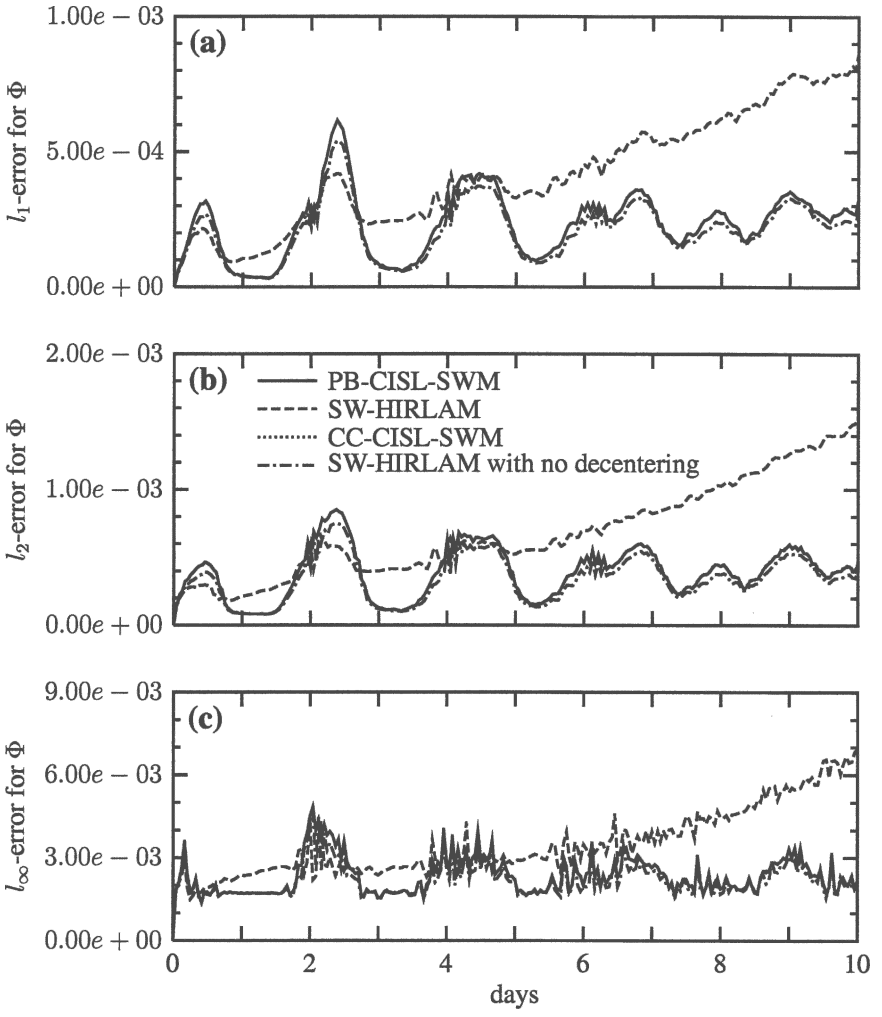

FIG. 6. Standard nondimensional error measure (a) l_1, (b) l_2, and (c) l_∞ for the geopotential height as a function of time for test case 5 when using the (dashed line) SW-HIRLAM, (dashed–dotted line) SW-HIRLAM without decentering, (solid line) PB-CISL-SWM, and (dotted line) CC-CISL-SWM. The x axis is the same for all plots. The time step is 30 min, which corresponds to a maximal Courant number of approximately five. The boundary field is updated at every time step using the reference solution. The error measures for the CISL models are indistinguishable on the figure.

of the mountain, which suddenly is raised in the balanced flow. This creates an initial imbalance that excites gravity waves.

The gravity waves excited by the imbalance in the initial condition will complete one revolution in approximately 44 h. The phase and amplitude of the gravity waves in the global reference solution and in the LAM numerical solutions are not identical due to the boundary relaxation and the model's representation of the gravity waves. Therefore, we see extrema in the error measures approximately every second day when gravity waves enter the domain (see Fig. 6). Since Φ_{00} is large in the CISL models, they perform worse than SW–HIRLAM as the gravity waves sweep through the domain. Otherwise the cell-integrated models perform much better than SW–HIRLAM while the cell-integrated models perform equally well. When not using decentering in the SW–HIRLAM the accuracy is comparable to the CISL models.

d. Rossby–Haurwitz wave (test case 6)

The initial condition is a Rossby–Haurwitz wave with wavenumber 4. The problem has an analytic solution for the nonlinear barotropic vorticity equation on the sphere but not for the nonlinear shallow-water equations. It was previously believed that wavenumber 4 is

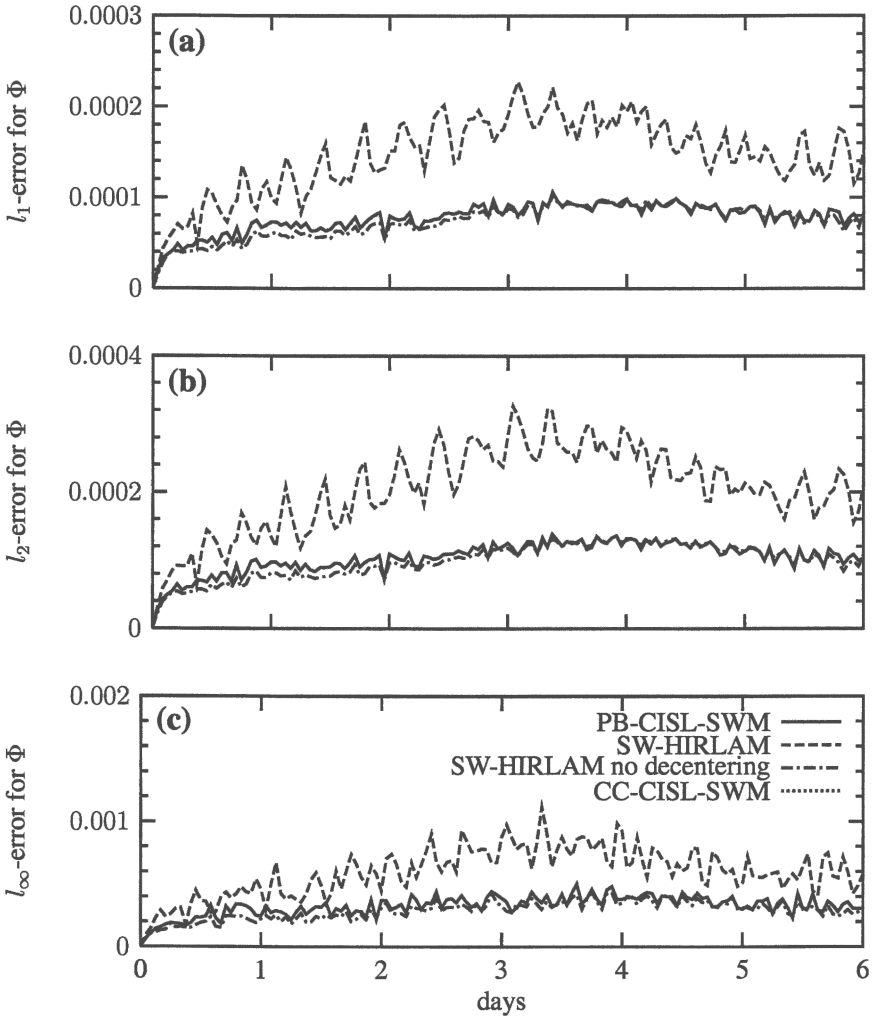

FIG. 7. Same as Fig. 6 but for test case 6 and a time step of 12 min. The error measures for the CISL models are indistinguishable on the figure.

stable (Hoskins 1973), but Thuburn and Li (2000) have shown that if a perturbation is introduced, small-scale features develop in the vorticity field due to an instability of the flow. This, of course, questions the accuracy of the reference solution. Sufficient diffusion of the numerical method or explicitly added diffusion tends to suppress the instability. However, for the high-resolution models used in Thuburn and Li (2000), which include the spectral model used here, the dynamical instability first shows by day 10 of the simulation. Hence, for the test runs here, which are less than 10 days, the instability may not degrade the accuracy of the reference solution.

It is difficult to argue that some region has more activity than others. Therefore, the LAM grid is chosen to coincide with the geographical latitude–longitude grid.

The Rossby–Haurwitz wave propagates slowly eastward with small vacillations about the steady propagating wave structure. The error measures for the different models are shown in Fig. 7. The numerically simulated wave propagates with a phase speed close to the one predicted by the nondivergent barotropic model. The noise in the error measures is primarily due to the vacillations. The CISL models are as accurate as the SW–HIRLAM without decentering. The SW–HIRLAM with decentering, however, performs significantly worse than all other model configurations.

e. Analyzed 500-mb height and wind field initial conditions (test case 7)

Three different initial conditions for the 500-mb height and winds were proposed in W92. These initial

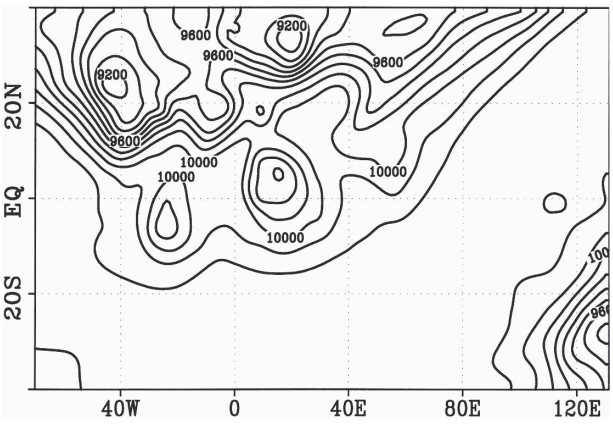

FIG. 8. The initial height field in meters on the LAM grid for test case 7. The rotated south pole is located at 40°S, 0°, and the axis labels denote position in the rotated grid. The contour interval is 100 m.

conditions were chosen more or less randomly and in this context there is no particular reason for choosing one of the situations over the others. Here the initial data from UTC9 January 1979 are used and the limited area is placed where a blocking develops (see Fig. 8).

The error measures are shown in Fig. 9. The CISL models perform better than the traditional model with respect to l_1 and l_2. Also, l_3 is slightly larger for the CISL models up to about day 4 after which the CISL models clearly perform better.

f. Computational cost

Ultimately the efficiency of using CISL schemes may only be discussed in full-blown 3D models implemented in multiprocessing environments. However, the horizontal part of a 3D hydrostatic model is similar to a shallow-water system, so it is important to discuss how the efficiency is affected by going from passive CISL advection to a semi-implicit CISL shallow-water model and to discuss the differences in the two CISL models tested here.

The CISL models have been implemented within the framework of the HIRLAM code without any attempts to optimize the code. The SW–HIRLAM code, however, is optimized and it would therefore make little sense to compare the actual CPU times for the two types of models. The computational cost for the momentum equations and the elliptic equation solver is identical for all model configurations. The explicit continuity equation is solved more efficiently using the CC-CISL scheme compared to the traditional method and less efficiently with the PB-CISL scheme. In general, the CISL schemes use more memory than conventional methods but that would have little effect on execution time on massively parallel computers since the extra memory usage consists of local information only. Computation of the correction term is not needed for the traditional system. The correction term is computed very efficiently with the PB-CISL scheme since the departure cell area is defined explicitly in terms of the departure points. In the CC-CISL scheme the intersection between the Lagrangian latitudes and Eulerian longitudes must be computed in order to define the departure cell geometry, which reduces the computational advantage the CC-CISL scheme has over the PB-CISL scheme for explicit advection. Weighing these differences, a small computational overhead for the CISL models compared to the conventional model is expected for an efficient implementation. With the present coding, it is not possible to decide about the relative efficiency of the two CISL models.

4. Possible extensions to a global domain

The model presented here is for a limited area, and for wider applications, an extension to a global domain is, of course, important. We suggest two methods to extend the model to a global domain. One extension uses a global latitude–longitude grid, which requires a certain amount of "engineering" and approximations near the poles. Perhaps a more viable approach to avoid the pole problem is to use the so-called Yin-Yang grid for spherical geometry (Kageyama and Sato 2004). We shall comment on each of these possibilities.

The first extension suggested requires the momentum equations be solved on vector form rather than on component form to avoid instability near the poles (e.g., Ritchie and Beaudoin 1994). In addition, the half-implicit Coriolis scheme must be replaced by a fully implicit scheme, and a vector form trajectory algorithm must be used. Then the semi-implicit CISL scheme for the continuity equation must be extended to a global domain.

Both CISL advection schemes used here have originally been formulated on the sphere and both use the same local approach for accurate transport over the polar regions, which allows for large meridional Courant numbers (NM02). In the vicinity of the poles, a high-resolution tangent plane is introduced. Apart from the two cells that include the Eulerian poles, the departure cells are "well defined" on the tangent plane and the remapping is formally equivalent to the regular case. For the polar singularity, a "latitudinal" belt of Lagrangian cells that contains the Eulerian pole, referred to as the "singular belt," is defined. The total mass inside the singular belt can be computed using the

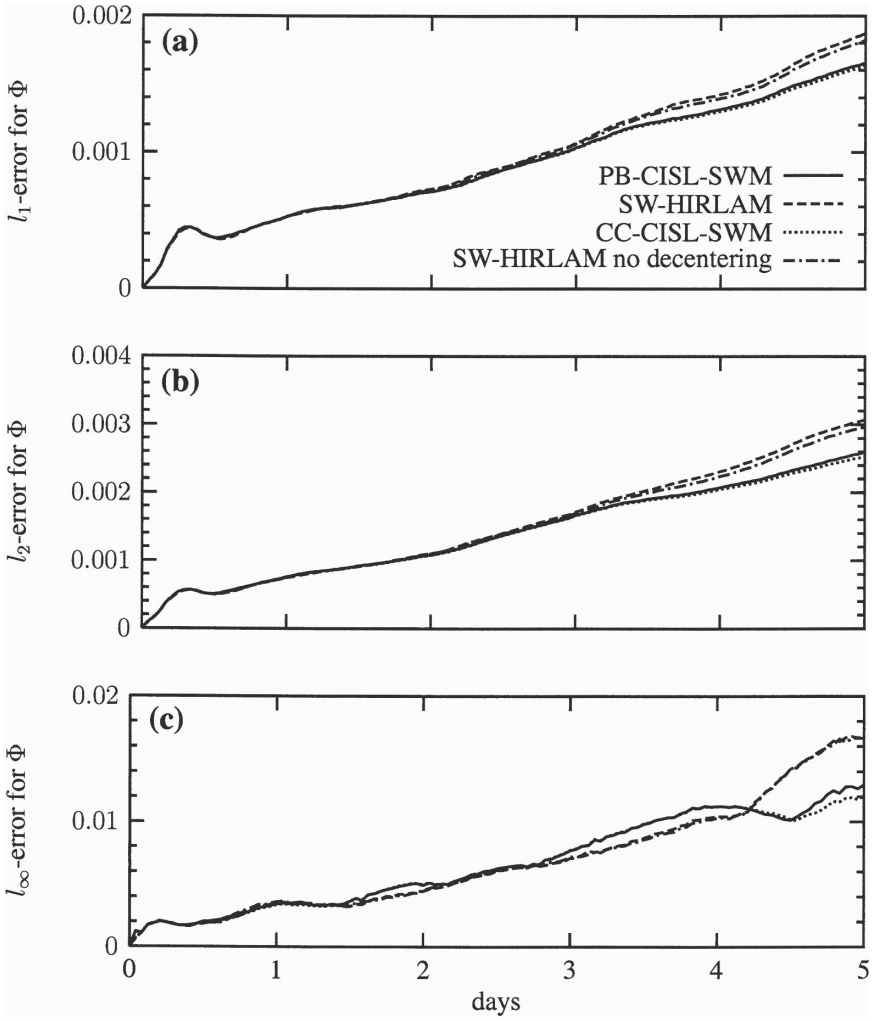

FIG. 9. Same as Fig. 6, but for test case 7 and a time step of 24 min.

regular algorithm on the tangent plane. Thereafter the total mass is approximately distributed to each cell using the weights equal to the mass at the midpoints of each cell computed by the traditional semi-Lagrangian method.

To extend the treatment of the polar regions used in the CISL advection schemes to the semi-implicit ones, the Lagrangian divergence must be computed. Apart from the singular belt, the departure cells are well defined and the Lagrangian divergence is easily computed. For the singular belt, the extension is also rather straightforward. An approach could be to advect a nonzero constant. Then the divergence will be readily available since the deviation from constancy is proportional to the change in area. So using the same method of distribution of mass in the singular belt outlined above also the divergence can be made available. Hence, theoretically we see no obvious obstacles in extending the limited-area model to a global domain using this approach but it does imply some algorithmic complexity.

Alternatively, the pole problem can be addressed by using the yin-yang grid recently developed for spherical geometry. This orthogonal grid is based on the overset grid methodology, that is, two overlapping subgrids where each subgrid is a spherically rotated latitude–longitude grid. Thus, effectively two LAMs are coupled. Hence, the model presented here can be applied without modifications on each subgrid. The pole problem is avoided at the expense of introducing an overlap region. This region is, however, static, and mass in the interface region can be conservatively remapped using an approach such as the pseudo-piecewise-parabolic method used here in one of the CISL model versions. A problem that must be solved is how to couple the elliptic systems of the two LAMs.

5. Summary

Two versions of a semi-implicit, semi-Lagrangian shallow-water model, which guarantees mass conservation by using cell-integrated methods for the continuity equation, have been developed. The two versions differ in the definition of their departure areas and in their subgrid-scale representations. The version based on the NM02 scheme uses a pseudo-biparabolic representation, which is the sum of two 1D piecewise parabolic functions along the Eulerian longitudes and latitudes. The version based on the advection scheme of Nair et al. (2002) uses a cascade approach with two successive remappings using 1D parabolic representations along Eulerian longitudes and Lagrangian latitudes, respectively. The mass is conserved locally in both versions and there is no need for ad hoc a posteriori mass-fixing algorithms as is the case for traditional semi-Lagrangian models. The cell-integrated models are efficient since they permit large time steps and their elliptic equation is on the same form as for the traditional semi-Lagrangian system and is relatively inexpensive to solve. In addition, desirable properties such as monotonicity and positive definiteness can easily be enforced.

The accuracy of the model has been assessed using selected test cases from the suite of test cases proposed by W92. For passive tracer advection the conservative transport schemes are much more accurate than traditional semi-Lagrangian methods. We believe that additional advantages of these models will be revealed in three-dimensional applications where they will guarantee consistency between a conservative transport of total mass and a conservative mass transport of individual tracers. The lack of such a consistency will generally violate the mass conservation of tracers (Jöckel et al. 2001).

For shallow-water model runs the accuracy and efficiency of the new models was estimated to be comparable to traditional semi-Lagrangian models. In all test cases, the cell-integrated models performed better than the traditional semi-Lagrangian method with decentering. The shallow-water tests performed revealed no clear difference in the accuracy of the two conservative model versions.

Acknowledgments. The first author carried out part of this research while visiting NCAR and is grateful to NCAR staff, in particular Ramachandran D. Nair and David L. Williamson, for helpful suggestions and useful discussions as well as assisting in clarifying parts of the manuscript. We thank two anonymous reviewers for their helpful comments. The research has been carried out within the framework of the Copenhagen Global Change Initiative (COGCI).

APPENDIX A

List of Acronyms

CISL	Cell-integrated semi-Lagrangian
CC-CISL	Conservative cascade cell-integrated semi-Lagrangian
CC-CISL-SWM	Conservative cascade cell-integrated semi-Lagrangian shallow-water model
ECMWF	European Centre for Medium-Range Weather Forecasts
HIRLAM	High Resolution Limited Area Model
LAM	Limited area model
M	Monotone
P	Positive definite
PB-CISL	Pseudo-biparabolic cell-integrated semi-Lagrangian
PB-CISL-SWM	Pseudo-biparabolic cell-integrated semi-Lagrangian shallow-water model
SETTLS	Stable extrapolation two-time-level scheme
SISL	Semi-implicit semi-Lagrangian
SM	Semi-monotone
SW-HIRLAM	Shallow-water version of the HIRLAM
TRAD	Traditional semi-Lagrangian

APPENDIX B

Linear and Nonlinear Terms

In spherical coordinates the linear and nonlinear terms are given by

$$L_u = f_0 v - \frac{1}{a\cos\theta}\frac{\partial}{\partial\lambda}(\Phi + \Phi_s), \tag{B1}$$

$$L_v = -f_0 u - \frac{1}{a}\frac{\partial}{\partial\theta}(\Phi + \Phi_s), \tag{B2}$$

$$L_\Phi = -\Phi_{00} D, \tag{B3}$$

$$N_u = f' v + \frac{uv}{a}\tan\theta, \tag{B4}$$

$$N_v = -f' u - \frac{u^2}{a}\tan\theta, \tag{B5}$$

$$N_\Phi = -(\Phi - \Phi_{00})\nabla\cdot\mathbf{v}, \tag{B6}$$

where the half-implicit Coriolis scheme (McDonald and Haugen 1992) has been used; that is, the Coriolis parameter is split into a constant part and the deviation from the constant, $f = f_0 + f'$. For discretization details see Undén (2002).

REFERENCES

Arakawa, A., and V. Lamb, 1977: Computational design and the basic dynamical processes of the UCLA general circulation model. *Methods Comput. Phys.,* **17,** 173–265.

Bermejo, R., and A. Staniforth, 1992: The conversion of semi-Lagrangian advection schemes to quasi-monotone schemes. *Mon. Wea. Rev.,* **120,** 2622–2632.

——, and J. Conde, 2002: A conservative quasi-monotone semi-Lagrangian scheme. *Mon. Wea. Rev.,* **130,** 423–430.

Colella, P., and P. R. Woodward, 1984: The piecewise parabolic method (PPM) for gas-dynamical simulations. *J. Comput. Phys.,* **54,** 174–201.

Davies, H., 1976: A lateral boundary formulation for multi-level prediction models. *Quart. J. Roy. Meteor. Soc.,* **102,** 405–418.

Dukowicz, J. K., and J. R. Baumgardner, 2000: Incremental remapping as a transport/advection algorithm. *J. Comput. Phys.,* **160,** 318–335.

Durran, D. R., and P. A. Reinecke, 2004: Instability in a class of explicit two-time-level semi-Lagrangian schemes. *Quart. J. Roy. Meteor. Soc.,* **130,** 365–369.

Gravel, S., and A. Staniforth, 1994: A mass-conserving semi-Lagrangian scheme for the shallow-water equations. *Mon. Wea. Rev.,* **122,** 243–248.

Hortal, M., 2002: The development and testing of a new two-time-level semi-Lagrangian scheme (SETTLS) in the ECMWF forecast model. *Quart. J. Roy. Meteor. Soc.,* **128,** 1671–1687.

Hoskins, B. J., 1973: Stability of the Rossby–Haurwitz wave. *Quart. J. Roy. Meteor. Soc.,* **99,** 723–745.

Jakob, R., J. Hack, and D. Williamson, 1993: Solutions to shallow water test set using the spectral transform method. NCAR Tech. Rep. TN-388+STR, 82 pp.

Jöckel, P., R. von Kuhlmann, M. G. Lawrence, B. Steil, C. Brenninkmeijer, P. J. Crutzen, P. J. Rasch, and B. Eaton, 2001: On a fundamental problem in implementing flux-form advection schemes for tracer transport in 3-dimensional general circulation and chemistry transport models. *Quart. J. Roy. Meteor. Soc.,* **127,** 1035–1052.

Kaas, E., 1987: The construction of and tests with a multi-level, semi-Lagrangian and semi-implicit limited area model. M.S. thesis, Geophysics Institute, University of Copenhagen, 114 pp.

——, P. H. Lauritzen, and B. Machenhauer, 2005: A shallow water model based on an accurate cell-integrated semi-Lagrangian and semi-implicit scheme. Danish Climate Center Rep. 05-02, Danish Meteorological Institute, Copenhagen, Denmark, 31 pp.

Kageyama, A., and T. Sato, 2004: The "yin-yang grid": An overset grid in spherical geometry. *Geochem. Geophys. Geosyst.,* **5,** Q09005, doi:10.1029/2004GC000734.

Källén, E., 1996: HIRLAM documentation manual. Swedish Meteorological and Hydrological Institute, 241 pp. [Available from SMHI, S-601 76 Norrköping, Sweden.]

Kwizak, M., and A. Robert, 1971: A semi-implicit scheme for grid point atmospheric models of the primitive equations. *Mon. Wea. Rev.,* **99,** 32–36.

Laprise, J., and A. Plante, 1995: A class of semi-Lagrangian integrated-mass (SLIM) numerical transport algorithms. *Mon. Wea. Rev.,* **123,** 553–565.

Lin, S.-J., 2004: A "vertically Lagrangian" finite-volume dynamical core for global models. *Mon. Wea. Rev.,* **132,** 2293–2307.

——, and R. Rood, 1996: Multidimensional flux-form semi-Lagrangian transport schemes. *Mon. Wea. Rev.,* **124,** 2046–2070.

Machenhauer, B., and M. Olk, 1997: The implementation of the semi-implicit scheme in cell-integrated semi-Lagrangian models. *Numerical Methods in Atmospheric and Oceanic Modelling: The André J. Robert Memorial Volume,* C. Lin, R. Laprise, and H. Ritchie, Eds., CMOS/NRC Research Press, 103–126.

——, and ——, 1998: Design of a semi-implicit cell-integrated semi-Lagrangian model. Max Planck Institute for Meteorology Tech. Rep. 265, Hamburg, Germany, 95 pp.

McDonald, A., 1999: An examination of alternative extrapolations to find the departure point position in a "two-time-level" semi-Lagrangian integration. *Mon. Wea. Rev.,* **127,** 1985–1993.

——, and J. Bates, 1989: Semi-Lagrangian integration of a gridpoint shallow water model on the sphere. *Mon. Wea. Rev.,* **117,** 130–137.

——, and J. Haugen, 1992: A two-time-level, three-dimensional semi-Lagrangian, semi-implicit, limited-area gridpoint model of the primitive equations. *Mon. Wea. Rev.,* **120,** 2603–2621.

——, and J. E. Haugen, 1993: A two time-level, three-dimensional, semi-Lagrangian, semi-implicit, limited-area gridpoint model of the primitive equations. Part II: Extension to hybrid vertical coordinates. *Mon. Wea. Rev.,* **121,** 2077–2087.

McGregor, J. L., 1993: Economical determination of departure points for semi-Lagrangian models. *Mon. Wea. Rev.,* **121,** 221–230.

Moorthi, S., R. Higgins, and J. Bates, 1995: A global multilevel atmospheric model using a vector semi-Lagrangian finite-difference scheme. Part II: Version with physics. *Mon. Wea. Rev.,* **123,** 1523–1541.

Nair, R. D., and B. Machenhauer, 2002: The mass-conservative cell-integrated semi-Lagrangian advection scheme on the sphere. *Mon. Wea. Rev.,* **130,** 649–667.

——, J. Côté, and A. Staniforth, 1999: Monotonic cascade interpolation for semi-Lagrangian advection. *Quart. J. Roy. Meteor. Soc.,* **125,** 197–212.

——, J. S. Scroggs, and F. H. M. Semazzi, 2002: Efficient conservative global transport schemes for climate and atmospheric chemistry models. *Mon. Wea. Rev.,* **130,** 2059–2073.

Priestley, A., 1993: A quasi-conservative version of the semi-Lagrangian advection scheme. *Mon. Wea. Rev.,* **121,** 621–632.

Purser, R., and L. Leslie, 1991: An efficient interpolation procedure for high-order three-dimensional semi-Lagrangian models. *Mon. Wea. Rev.,* **119,** 2492–2498.

Rančić, M., 1992: Semi-Lagrangian piecewise biparabolic scheme for two-dimensional horizontal advection of a passive scalar. *Mon. Wea. Rev.,* **120,** 1394–1405.

——, 1995: An efficient, conservative, monotonic remapping for semi-Lagrangian transport algorithms. *Mon. Wea. Rev.,* **123,** 1213–1217.

Ritchie, H., and C. Beaudoin, 1994: Approximations and sensitivity experiments with a baroclinic semi-Lagrangian spectral model. *Mon. Wea. Rev.,* **122,** 2391–2399.

Rivest, C., A. Staniforth, and A. Robert, 1994: Spurious resonant response of semi-Lagrangian discretizations to orographic forcing: Diagnosis and solution. *Mon. Wea. Rev.,* **122,** 366–376.

Robert, A., 1969: The integration of a spectral model of the atmosphere by the implicit method. *Proc. WMO/IUGG Symp. on Numerical Weather Prediction,* Tokyo, Japan, Japan Meteorological Agency, VII.19–VII.24.

——, 1981: A stable numerical integration scheme for the primitive meteorological equations. *Atmos.–Ocean,* **19,** 35–46.

——, 1982: A semi-Lagrangian and semi-implicit numerical integration scheme for the primitive meteorological equations. *J. Meteor. Soc. Japan,* **60,** 319–325.

——, J. Henderson, and C. Turnbull, 1972: An implicit time integration scheme for baroclinic models of the atmosphere. *Mon. Wea. Rev.,* **100,** 329–335.

Simmons, A. J., and C. Temperton, 1997: Stability of a two-time-level semi-implicit integration scheme for gravity wave motion. *Mon. Wea. Rev.,* **125,** 600–615.

Staniforth, A., and J. Côté, 1991: Semi-Lagrangian schemes for atmospheric models—A review. *Mon. Wea. Rev.,* **119,** 2206–2223.

Temperton, C., and A. Staniforth, 1987: An efficient two-time-level semi-Lagrangian semi-implicit integration scheme. *Quart. J. Roy. Meteor. Soc.,* **113,** 1025–1039.

Thuburn, J., and Y. Li, 2000: Numerical simulations of Rossby–Haurwitz waves. *Tellus,* **52A,** 181–189.

Undén, P., 2002: HIRLAM-5 scientific documentation. Swedish Meteorological and Hydrological Institute, 144 pp. [Available from SMHI, S-601 76 Norrköping, Sweden.]

Williamson, D., J. Drake, J. Hack, R. Jakob, and P. Swarztrauber, 1992: A standard test set for numerical approximations to the shallow water equations in spherical geometry. *J. Comput. Phys.,* **102,** 211–224.

Zerroukat, M., N. Wood, and A. Staniforth, 2004: SLICE-S: A semi-Lagrangian inherently conserving and efficient scheme for transport problems on the sphere. *Quart. J. Roy. Meteor. Soc.,* **130,** 2649–2664.

——, ——, and ——, 2005: A monotonic and positive-definite filter for a semi-Lagrangian inherently conserving and efficient (SLICE) scheme. *Quart. J. Roy. Meteor. Soc.,* **131,** 2923–2936.